Asymptotic Full Wave-Form Inversion in the Image Domain

Maxim Protasov(✉)

Institute of Petroleum Geology and Geophysics, Koptyug st. 3, Novosibirsk 630090, Russia
protasovmi@ipgg.sbras.ru

Abstract. This study considers the Full Waveform Inversion (FWI) method in the image domain based on the asymptotic solution of the Helmholtz equation. The paper provides ray tracing and beam migration to get the images used to compute the tomographic part of the asymptotic FWI gradient. The comparison of asymptotic FWI and Common Image Point (CIP) tomography show that the computational time for both methods is similar while they provide reconstruction of different model parts. A series of numerical experiments show that CIP tomography is effective in reconstructing the low frequency model, while asymptotic FWI provides recovery of the details of complex velocity structure.

Keywords: full wave-form inversion · asymptotic solution · image domain · tomography

1 Introduction

Exploration and production of new oilfields is one of the most important and toughest challenges that geosciences have ever faced. In recent years, the most accessible and well-studied areas of oilfield production are coming to their end. Exploration of new resources has to be carried in regions with severe environments and complex geological conditions. In such areas, there is a strong demand for new methods of acquisition and processing of seismic data, which should allow to record and retrieve as much as possible reliable information about the structure of the subsurface. One of the potential approach for improving depth-velocity models in areas with complex geology is a full wave-form inversion technique, which seeks the solution of seismic inverse problem by minimizing the least-squares misfit between the observed and the simulated data [1, 2].

The full wave-form inversion approach has got successful applications in several studies using computationally expensive finite difference methods [3, 4] and finite element methods [5]. Modern implementations of FWI attempt to recover a sufficiently broad spatial spectrum of the model. Examples of wide azimuth data illustrate the possibility of recovering all spatial spectrums of the medium [6]. Some of the recent researches have investigated multi-parameter FWI [7], and FWI solutions in complex models, for example, containing high contrast salt bodies [8]. Another important direction for providing new solutions is based on the application of accurate forward modeling techniques [9].

© The Author(s), under exclusive license to Springer Nature Switzerland AG 2024
O. Gervasi et al. (Eds.): ICCSA 2024, LNCS 14813, pp. 255–267, 2024.
https://doi.org/10.1007/978-3-031-64605-8_18

However, FWI has essential limitations in practical application, and the motivation of the presented paper is to provide solutions that allow overcoming these limitations. There are two main reasons for these limitations: the computational cost and the quality of seismic data. The main computation cost of FWI is a direct result of the numerical modeling of seismic wave-fields. Therefore, the development of methods for numerical modeling of seismic wave-fields and the acceleration of algorithms for such modeling is an extremely urgent task. Asymptotic methods are much faster than finite difference or finite element methods, which are used in most of the developed inversion algorithms. Therefore, in the previous work [10], the authors demonstrate the practical computational benefits and possibilities of the asymptotic FWI in the data frequency domain, and show that it can be practically useful. However, the success of the full wave-from inversion is very sensitive to the quality of the registered data, and it is almost impossible to satisfy the requirements of this approach, for example, in areas with complex near-surface conditions. It comes from the standard implementation of FWI in the data domain, while the potential solution can be the inversion of seismic wave-fields in the image domain [11] where the signal-to-noise ratio is much higher.

Therefore, in this paper, we propose to perform the inversion of seismic wave-fields in the image domain, contrary to the classical full wave-form inversion, which is done in data domain. The key point which we use for wave-form inversion is a wave-field modeling and imaging scheme based on asymptotic wave-equation solutions constructed using Gaussian beams summation. This allows achieving very high signal-to-noise ratio because of the massive directional summation of data for each imaging point. Also, the proposed asymptotic modeling scheme should work much faster and efficiently than the classically used methods for full-waveform inversion based on finite differences or finite elements solutions. Together, the combination of such modeling and migration procedure and inversion in the image domain should provide a robust method for imaging and inversion of seismic wave fields in areas with complex geology. In order to investigate the proposed inversion scheme and to understand its benefits and drawbacks in details we provide the realization of the proposed approach and its numerical investigation on a realistic Marmousi model.

2 Asymptotic Full Wave-Form Inversion: Theory

2.1 Full Wave-Form Inversion in the Image Domain

The acoustic media is considered, and the wave field in the frequency domain $u(x, z; \omega)$ satisfies the Helmholtz equation:

$$\left(\Delta + \omega^2 m\right) u = -f(\omega)\delta(x - x_s)\delta(z - z_s), \tag{1}$$

here $m = c^{-2}(x, z)$ is the square of slowness, and $c(x, z)$ is the wave propagation velocity, $f(\omega)$ is the wavelet at the source in the frequency domain, ω is the frequency, (x_s, z_s) is the source coordinate.

Then, introduce an operator that computes the wave field from a single point source for a fixed frequency at points corresponding to the receiver locations. Thus, the following

forward modeling operator is obtained:

$$\mathrm{F} : \mathrm{M} \to \mathrm{D}, \tag{2}$$

where D is the data space, M is the model space. In these notations, the inverse dynamic problem of constructing a velocity model from seismic data reduces to solving a nonlinear operator equation:

$$\mathrm{d}^{\mathrm{obs}} = \mathrm{F}(\mathrm{m}_{\mathrm{true}}), \tag{3}$$

here $\mathrm{d}^{\mathrm{obs}}$ is the observed data, $\mathrm{m}_{\mathrm{true}}$ is the true velocity model.

Full-wave inversion in the image domain minimizes the functional built in the image domain:

$$\mathrm{m}_* = \arg\left(\min_{\mathrm{m}\in\mathrm{M}} \|\mathrm{M} < \mathrm{F}(\mathrm{m}) - \mathrm{d} > \|_{\mathrm{I}}^2\right). \tag{4}$$

Here, M is the migration operator, which transfers the data to the image domain I, where the minimization takes place. To do this, we use migration on Gaussian beams [12]:

$$\mathrm{M} < \mathrm{d} > (\mathrm{y}, \mathrm{p}) = \sum\nolimits_{x_s, x_r, \omega} T^m_{gbs}(x_s; y, p; \omega) \cdot T^m_{gbr}(x_r; y, p; \omega) \cdot \mathrm{d}(x_s, x_r, \omega). \tag{5}$$

Here $\mathrm{T}^m_{\mathrm{gbs}}(\mathrm{x_s}; \mathrm{y}, \mathrm{p}; \omega)$, $\mathrm{T}^{\mathrm{m}}_{\mathrm{gbr}}(\mathrm{x_r}; \mathrm{y}, \mathrm{p}; \omega)$ are the summation weights of the migration operator M [12].

When using local optimization methods, the key step is also the calculation of the gradient, which in this case has the following representation:

$$\nabla_{\mathrm{k}}(\mathrm{x}) = \mathrm{Re}\left\{\sum\nolimits_{\mathrm{y,p}} \delta Image_{\mathrm{k}}(\mathrm{y}, \mathrm{p}) \cdot \left(\frac{\partial \delta Image_{\mathrm{k}}(\mathrm{y}, \mathrm{p})}{\partial \mathrm{m}_\kappa(\mathrm{x})}\right)^*\right\}. \tag{6}$$

Here $\delta Image_{\mathrm{k}}(\mathrm{y}, \mathrm{p}) = \mathrm{Image}_{\mathrm{k}}(\mathrm{y}, \mathrm{p}) - \mathrm{Image}_{\mathrm{dk}}(\mathrm{y}, \mathrm{p})$ is the residual in the image domain, where $\mathrm{Image}_{\mathrm{dk}}(\mathrm{y}, \mathrm{p}) = \mathrm{M}_k < \mathrm{d} > (\mathrm{y}, \mathrm{p})$ and $\mathrm{Image}_{\mathrm{k}}(\mathrm{y}, \mathrm{p}) = \mathrm{M}_k < \mathrm{F}(\mathrm{m}_\kappa) > (\mathrm{y}, \mathrm{p})$:

$$\mathrm{Image}_{\mathrm{k}}(\mathrm{y}, \mathrm{p}) = \sum\nolimits_{x_s, x_r, \omega} T^{m_k}_{gbs}(x_s; y, p; \omega) \cdot T^{m_k}_{gbr}(x_r; y, p; \omega) \cdot \mathrm{F}(\mathrm{m}_\kappa)(x_s, x_r, \omega). \tag{7}$$

The derivative of the image misfit function has the following form:

$$\frac{\partial \delta Image_{\mathrm{k}}(\mathrm{y}, \mathrm{p})}{\partial \mathrm{m}_\kappa(\mathrm{x})} = \sum\nolimits_{\mathrm{s,r},\omega} \{\mathrm{T}^{\mathrm{m_k}}_{\mathrm{gbs}}(\mathrm{x_s}; \mathrm{y}, \mathrm{p}; \omega) \cdot \mathrm{T}^{\mathrm{m_k}}_{\mathrm{gbr}}(\mathrm{x_r}; \mathrm{y}, \mathrm{p}; \omega) \cdot \frac{\partial \mathrm{F}(\mathrm{m}_\kappa)(\mathrm{x_s}, \mathrm{x_r}, \omega)}{\partial \mathrm{m_k}(\mathrm{x})} +$$
$$+ [\frac{\partial \mathrm{T}^{\mathrm{m_k}}_{\mathrm{gbs}}(\mathrm{x_s}; \mathrm{y}, \mathrm{p}; \omega)}{\partial \mathrm{m_k}(\mathrm{x})} \cdot \mathrm{T}^{\mathrm{m_k}}_{\mathrm{gbr}}(\mathrm{x_r}; \mathrm{y}, \mathrm{p}; \omega) + \frac{\partial \mathrm{T}^{\mathrm{m_k}}_{\mathrm{gbr}}(\mathrm{x_r}; \mathrm{y}, \mathrm{p}; \omega)}{\partial \mathrm{m_k}(\mathrm{x})} \cdot \mathrm{T}^{\mathrm{m_k}}_{\mathrm{gbs}}(\mathrm{x_s}; \mathrm{y}, \mathrm{p}; \omega)] \cdot \mathrm{F}(\mathrm{m}_\kappa)\}. \tag{8}$$

It turns out that the gradient in the image domain is the sum of two components: an analogue of the gradient in the data domain and the part associated with the dependence of the migration operator on the model. Therefore, on the one hand, the FWI in the image domain should be more informative. On the other hand, it is more stable, since images have a better signal-to-noise ratio than seismic data.

2.2 Tomographic Part of Asymptotic Full Wave-Form Inversion in the Image Domain vs Common Image Point Tomography

Next, in the gradient (9) the data domain analogue is omitted, and the expression for the derivative of the image misfit function (11) is transformed, and the gradient gets the following asymptotic approximation:

$$\nabla_{\mathrm{k}}(\mathrm{x}) = \mathrm{Re}\left\{\sum\nolimits_{\mathrm{y,p}} \delta Image_{\mathrm{k}}(\mathrm{y,\,p}) \cdot \mathrm{Image}_k^{i\omega}(\mathrm{y,\,p}) \left[\frac{\partial \tau_s(y,p)}{\partial m_k(x)} + \frac{\partial \tau_r(y,p)}{\partial m_k(x)}\right]^*\right\}. \quad (9)$$

Here $\tau_s(y,p)$, $\tau_r(y,p)$ are travel times to sources and receivers, computed in the model m_k, from the point y, and $\mathrm{Image}_k^{i\omega}$ has the following expression:

$$\mathrm{Image}_k^{i\omega}(\mathrm{y,\,p}) = \sum\nolimits_{x_s,x_r,\omega} -i\omega \cdot T_{gbs}^{m_k}(x_s;\,y,\,p;\,\omega) \cdot T_{gbr}^{m_k}(x_r;\,y,\,p;\,\omega) \cdot \mathrm{F}(\mathrm{m}_\kappa). \quad (10)$$

The gradient (12) is similar to the gradient of the tomography operator because there are the travel time derivatives with respect to model parameters. Therefore, this part of the gradient is called a tomographic part of asymptotic full wave-form inversion in the image domain.

From another point of view, when considering the linear step of the full wave-form, one can come to the following asymptotic representation of the image misfit function containing only the tomographic part:

$$\delta Image_{\mathrm{k}}(\mathrm{y,\,p}) \approx \sum\nolimits_x \left[\frac{\partial \tau_s(y,p)}{\partial m_k(x)} + \frac{\partial \tau_r(y,p)}{\partial m_k(x)}\right] \mathrm{Image}_k^{i\omega}(\mathrm{y,\,p}) \langle \delta m_{\mathrm{k}}(x) \rangle. \quad (11)$$

The linear step of the reflection tomography problem provides the following expression:

$$\delta T(\mathrm{y,\,p}) \approx \sum\nolimits_x \left[\frac{\partial \tau_s(y,p)}{\partial m_k(x)} + \frac{\partial \tau_r(y,p)}{\partial m_k(x)}\right] \langle \delta m_{\mathrm{k}}(x) \rangle. \quad (12)$$

Here $\delta T(\mathrm{y,\,p})$ is the travel time residuals between observed reflected travel times and the computed in the model $m_k(x)$ travel times, which is the sum of $\tau_s(y,p)$, $\tau_r(y,p)$. One can observe the similarity of the expressions (11) and (12). For the tomography case, it has a tomographic operator in right-hand side and travel time residuals in left - hand side. For the asymptotic FWI case, the expression consists of the weighted tomographic operator in the right-hand side and image misfit in the left-hand side. This means the expression (11) is the dynamic analogue of the kinematic problem (12).

3 Numerical Experiments

3.1 Description of the Synthetic Marmousi Model and Data

Today, the standard has become the need to test any developed algorithm on synthetic models and data. To date, a fairly large number of synthetic data for realistic models. One of the most well-known datasets is the freely available Marmousi2 P-wave velocity model [13], one can observe the model on the Fig. 1a. The acoustic modeling using

the finite difference scheme for the wave equation provides seismic data. The dataset simulates a 2D line seismic survey, in which observations consist of 320 sources, and the distance between sources equals to 50 m. Each source provides a signal recorded by 81 receivers, the distance between the receivers equals to 25 m, and therefore the maximum source-receiver offset equals 4000 m. The modeling utilizes the Ricker impulse, the dominant frequency is 15 Hz. Figure 1b provides the example of the seismogram, the source position is at x = 500 m.

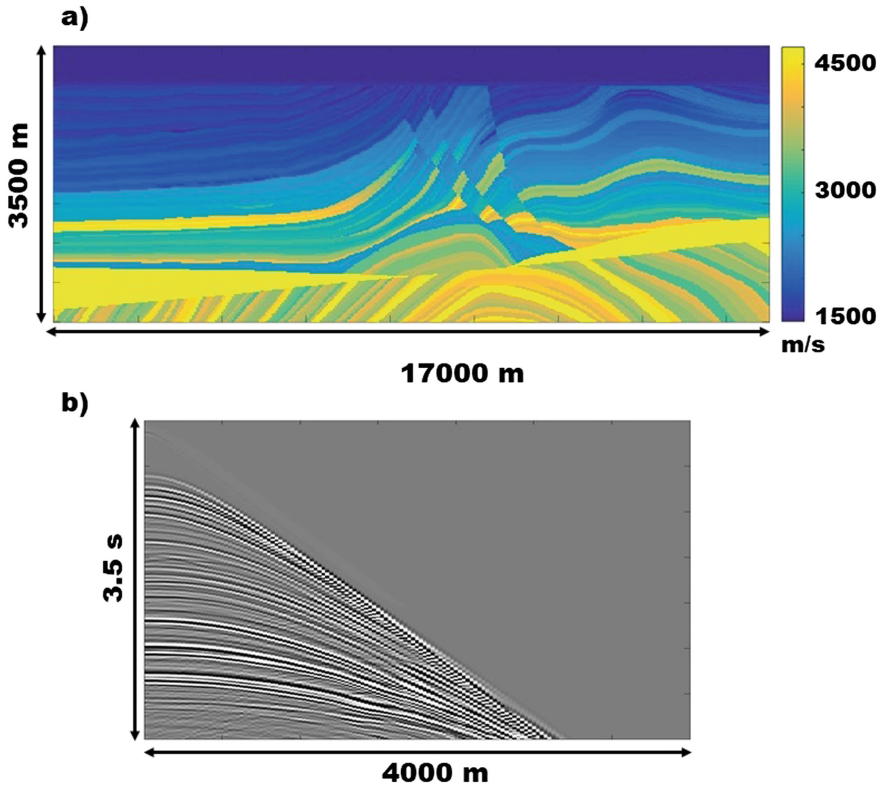


Fig. 1. (a) The original Marmousi2 model: P-wave velocity. (b) Seismogram got via finite-difference acoustic modeling in Marmousi2 model for the source position at x = 500 m.

3.2 Inversion Scenarios

For the investigation of the possibilities of proposed asymptotic FWI in the image domain, the inversion process uses different initial models. The investigation provides three essentially different scenarios.

In the first one, the initial model come from a reasonable 1D depth trend of the model and finally it represents a laterally homogeneous model (see Fig. 2a). This model has a big difference with the true model. In that model, the beam migration result shows the

highly defocused events and the essentially incorrect positions of the reflection interfaces, especially below the depth of 2500 m (see Fig. 2b).

For the second scenario, the initial model contains the lateral variations that come from the true model. The initial model is a strong smoothing of the true Marmousi model (see Fig. 3a). Here, the initial model has a smaller difference with the true Marmousi model in comparison with the initial model from the first scenario. However, the difference is still essential. The beam migration results in this case provide better focused events and more correct positions of the reflectors while they are still mis-positioned significantly (see Fig. 3b).

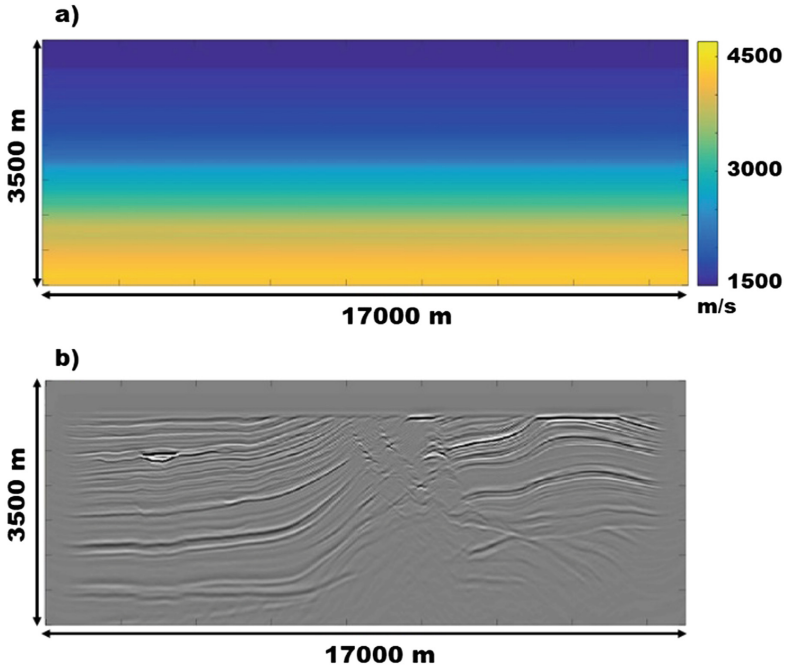


Fig. 2. (a) The initial laterally homogeneous model for the asymptotic FWI in the image domain: it has a big difference with the true Marmousi model. (b) The corresponding seismic image got via beam migration.

For the last scenario, the initial model is an average smoothing of the true Marmousi model (see Fig. 4a). Here, the initial model has no big difference with the true Marmousi model. But it does not contain the high-frequency component of the true model and it provides a sensible difference of the kinematic properties in comparison with the true model. The beam migration result in this model provides an image with reflectors positions that are close the true ones. However, there is slight difference in most of the model, and it becomes essential in the central most complex part of the model (see Fig. 4b).

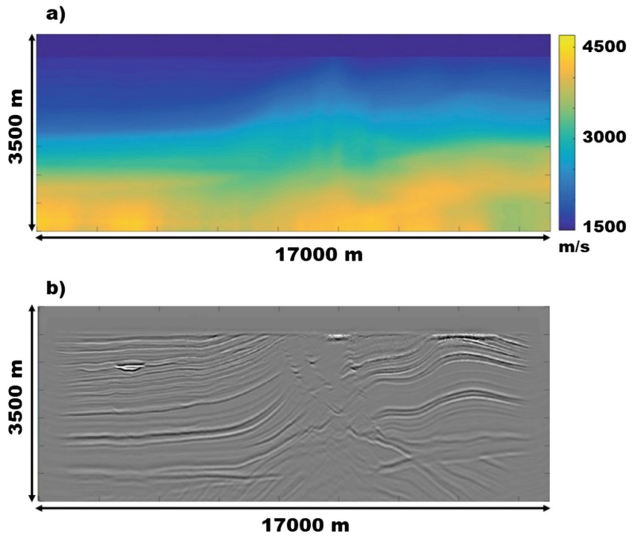


Fig. 3. (a) The initial highly smoothed Marmousi model for the asymptotic FWI in the image domain: it has an essential difference with the true Marmousi model. (b) The corresponding seismic image got via beam migration.

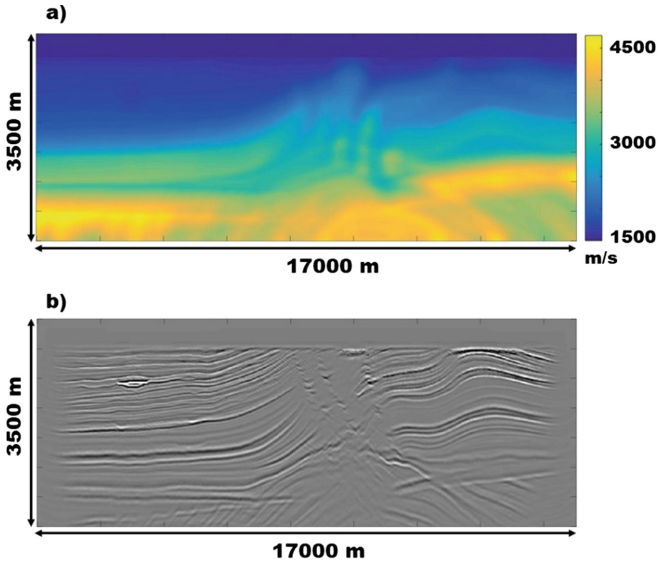


Fig. 4. (a) The initial averagely smoothed Marmousi model for the asymptotic FWI in the image domain: it has a reasonable difference with the true Marmousi model. (b) The corresponding seismic image got via beam migration.

3.3 Common Image Point Tomography Results

The first series of experiments provides the results of CIP tomography [14] application for the described above inversion scenarios. Such decision is logical because the liner step of CIP tomography has a similar statement of the Problem (Formula (15)) as the linear step of asymptotic FWI in the image domain (Formula (14)). Also, the input data (before picking the kinematic events in CIP tomography technology) are the same, and this data are the common image point seismograms i.e. migrated images for the different angle/offset parameters (defined by $\boldsymbol{p}$ in the Formulas (14) and (15)). It means that CIP tomography uses the kinematic properties of the migrated images, while the asymptotic FWI in the image domain uses dynamic properties of the same migrated images. Moreover, CIP tomography is a standard practical tool for the depth model reconstruction. Therefore, it is interesting to understand what can provide the proposed asymptotic FWI in the image domain in comparison with its kinematic analogue, i.e. CIP tomography.

Figures 5, 6 and 7 show the results of the linear step application of CIP tomography for the three described above correspondent scenarios. In those figures, the upper ones provide the inverted velocity model, while the bottom ones show the corresponding velocity update. One can observe that, for all three cases, the tomography provides the inverted model that becomes closer to the true model in comparison with the initial one. The most impressive result one can observe in the Fig. 5 for the first scenario when the initial model has a big difference with the true model. Here, the inverted model is similar to the smoothed Marmousi model shown in the Fig. 3a. However, for all 3 cases, the model update gives a rather smooth solution. This is an important observation, especially

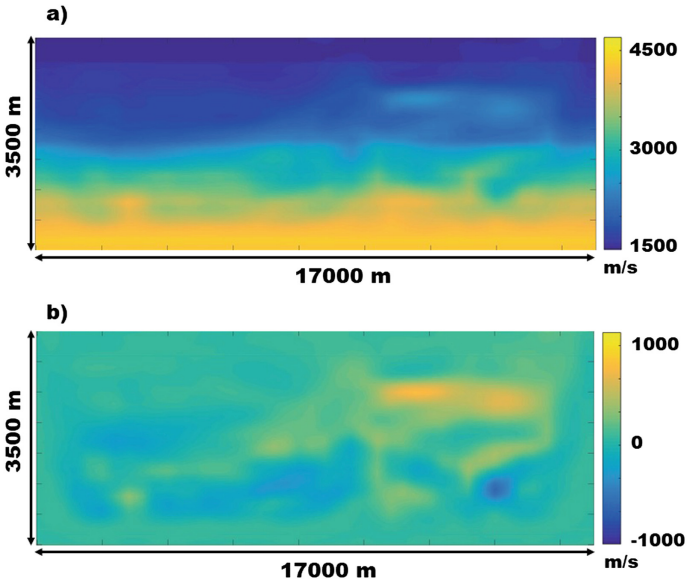


Fig. 5. (a) The result of the liner step of common image point tomography using the laterally homogeneous initial model. (b) The corresponding velocity update.

for the third scenario, when the migration model is close to the ideal. However, in this case, the tomography does not provide an update of fine structure, but still it gives the residual smooth part of the model.

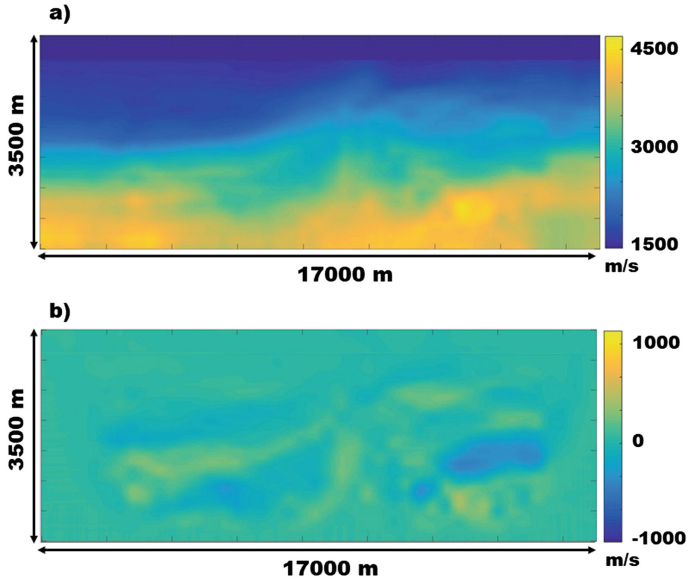


Fig. 6. (a) The result of the liner step of common image point tomography using the highly smoothed Marmousi initial model. (b) The corresponding velocity update.

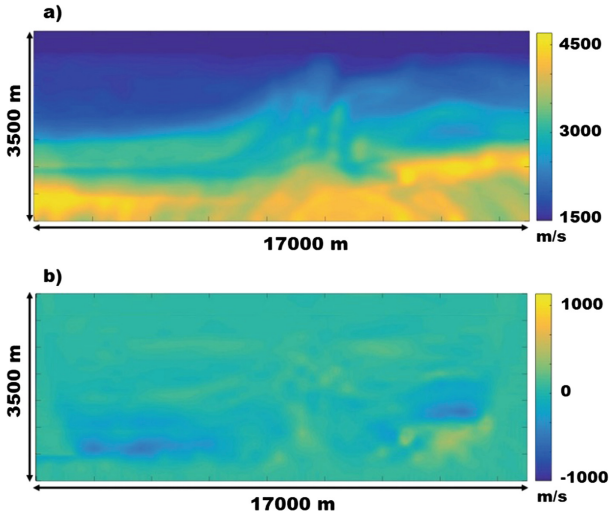


Fig. 7. (a) The result of the liner step of common image point tomography using the averagely smoothed Marmousi initial model. (b) The corresponding velocity update.

3.4 Results of Tomographic Part of Asymptotic FWI in the Image Domain

Finally, the proposed asymptotic FWI in the image domain is tested. Figures 8, 9 and 10 show the results of the linear step application of asymptotic FWI in the image for the three described above correspondent scenarios. On those figures, the upper ones provide the inverted velocity model, while the bottom ones show the corresponding velocity update. The computational time for all experiments is almost the same, and it equals to the computational time for CIP tomography experiments. It means that proposed asymptotic FWI in the image domain provides the computational speed up comparing to the standard FWI because it is well-known fact that CIP tomography is much faster than standard FWI approach. For example, computational cost of CIP tomography applied to real seismic data from the area around 1000 km^2 is estimated by days using rather powerful computational cluster, while computation cost of standard FWI based on finite-difference modelling is estimated by months on the same data and using the same computational cluster.

The results of the proposed asymptotic FWI in the image domain are different completely from the results of CIP tomography. One can observe that, for the first two scenarios, when the initial model has an essential difference with the true model the proposed FWI does not give the satisfactory inverted model result (Figs. 8 and 9). The explanation of such results consequence from the investigations for the time domain FWI, where the so-called cycle-skipping problem arises [15]. Because traces in the image domain are analogue to the traces in the time done, therefore image domain inherits this cycle-skipping problem.

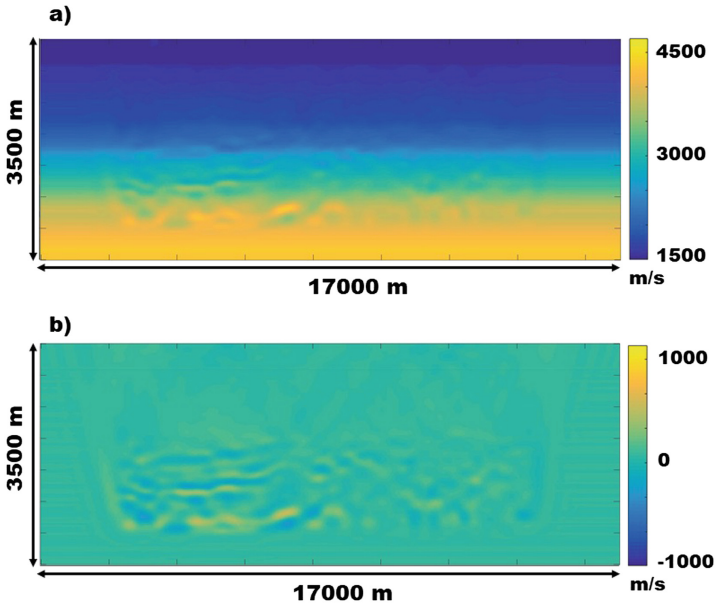


Fig. 8. (a) The result of liner step of the proposed asymptotic FWI in the image domain using the laterally homogeneous initial model. (b) The corresponding velocity update.

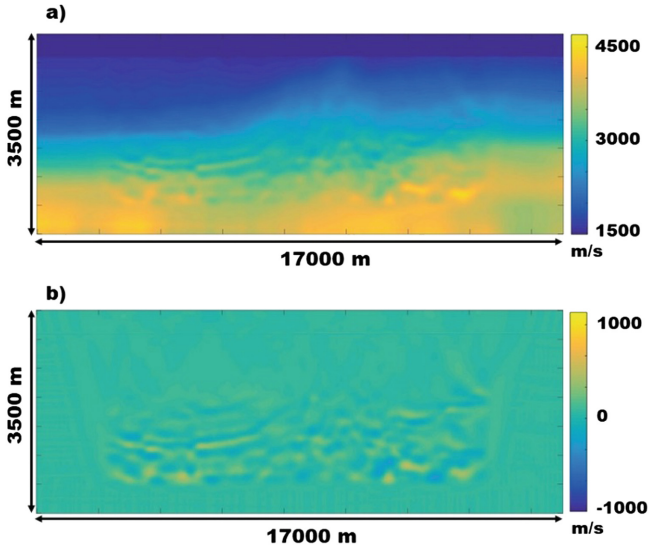


Fig. 9. (a) The result of liner step of the proposed asymptotic FWI in the image domain using the highly smoothed Marmousi initial model. (b) The corresponding velocity update.

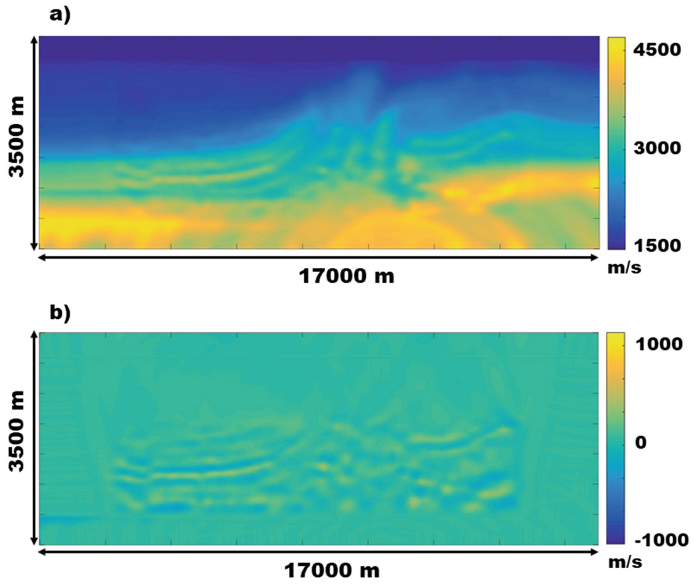


Fig. 10. (a) The result of the liner step of the proposed asymptotic FWI in the image domain using the averagely smoothed initial Marmousi model. (b) The corresponding velocity update.

The results of the proposed asymptotic FWI in the image domain for the third scenario show the model improvement (see Fig. 10). Here, the initial model is not very

different from the true model therefore, there is no influence of cycle-skipping problem. The reconstructed model is closer to the true model in comparison to the initial model used for the inversion. Here the model update (see Fig. 10b) contains higher frequency components comparing with the model update got by CIP tomography (see Fig. 7b). Here, asymptotic FWI in the image domain provides a more detailed model in comparison with the initial model and the recovered model by CIP tomography.

4 Conclusions

This work provides the new asymptotic full-wave inversion method in the image domain and its investigation. The classical FWI solution uses a computationally expensive procedure for the finite difference solution of the wave equation. The asymptotic approach uses ray tracing to solve wave equation, and migration on Gaussian beams to go to the image domain, which makes it possible to speed up the gradient construction procedure in comparison with the standard FWI. The comparison of asymptotic FWI and Common Image Point (CIP) tomography shows that the speed of calculations for both methods is similar, while CIP tomography is much faster than standard FWI approach. Also, the comparison shows that proposed asymptotic FWI and CIP tomography provide reconstruction of different model parts. A series of numerical experiments for a rather complex Marmousi model show that CIP tomography is effective in reconstructing low frequency model while asymptotic FWI provides recovery of the details of complex velocity structure.

Acknowledgements. The presented research is supported and done within the scope of investigations of RSF grant 21-71-20002. We use the computational resources of Peter the Great Saint-Petersburg Polytechnic University Supercomputing Center (scc.spbstu.ru) to provide the numerical experiments and to obtain the numerical results.

References

1. Lailly, P.: The seismic inverse problem as a sequence of before stack migrations. In: Conference on Inverse Scattering Theory and Application, pp. 206–220 (1983)
2. Tarantola, A.: Inversion of seismic reflection data in the acoustic approximation. Geophysics **49**, 1140–1395 (1984)
3. Pica, A., Diet, J., Tarantola, A.: Nonlinear inversion of seismic reflection data in laterally invariant medium. Geophysics **55**, 284–292 (1990)
4. Djikp'ess'e, H., Tarantola, A.: Multiparameter 1-norm waveform fitting: interpretation of Gulf of Mexico reflection seismograms. Geophysics **64**, 1023–1035 (1999)
5. Choi, Y., Min, D.-J., Shin, C.: Two-dimensional waveform inversion of multi-component data in acoustic-elastic coupled media. Geophys. Prospect. **56**, 863–881 (2008)
6. Pratt, R.G.: Seismic waveform inversion in the frequency domain, part 1: theory and verification in a physical scale model. Geophysics **64**, 888–901 (1999)
7. Luo, J., Wu, R.S., Chen, G.: Angle domain direct envelope inversion method for strong scattering velocity and density estimation. IEEE Geosci. Remote Sens. Lett. **17**, 1508–1512 (2020)

8. Chen, G., Yang, W.C., Liu, Y.N., Wang, H., Huang, X.: Salt structure elastic full waveform inversion based on the multi-scale signed envelope. IEEE Trans. Geosci. Remote Sens. **60**, 1–12 (2022)
9. Aghamiry, H.S., Gholami, A., Aghazade, K., Sonbolestan, M., Operto, S.: Large-scale highly-accurate extended full waveform inversion using convergent Born series. arXiv:2202.08558 (2022)
10. Protasov, M., Gadylshin, K., Neklyudov, D., Klimes, L.: Full waveform inversion based on an asymptotic solution of Helmholtz equation. Geosciences **13**, 1–13 (2023)
11. Zhang, S., Schuster, G.: Image-domain full waveform inversion: field data example. In: SEG Technical Program Expanded Abstracts, pp. 966–970 (2014)
12. Protasov, M., Tcheverda, V.: True amplitude imaging by inverse generalized Radon transform based on Gaussian beam decomposition of the acoustic Green's function. Geophys. Prospect. **59**, 197–209 (2011)
13. Martin, G.S., Wiley, R., Marfurt, K.J.: Marmousi2: an elastic upgrade for Marmousi. Lead. EdgeEdge **25**, 156–166 (2006)
14. Woodward, M., Nichols, D., Zdraveva, O., Whitfield, P., Johns, T.: A decade of tomography. Geophysics **73**, VE5-VE11 (2008)
15. Yang, J., Li, Y., Liu, Y., Wei, Y., Fu, H.: Mitigating the cycle-skipping of full-waveform inversion by random gradient sampling. Geophysics **85**, R493–R507 (2020)